

Enhanced thermal conductance at gold-amorphous silicon interfaces

Julien El Hajj,^{*} Gilles Ledoux, and Samy Merabia[†]

Univ Lyon, Univ Claude Bernard Lyon 1, CNRS, Institut Lumière Matière, F-69622, VILLEURBANNE, France

(Dated: January 19, 2024)

Heat transfer at the interface between two materials is becoming increasingly important as the size of electronic devices shrinks. Most studies concentrate on the interfacial thermal conductance between either crystalline-crystalline or amorphous-amorphous materials. Here, we investigate the interfacial thermal conductance at crystalline-amorphous interfaces using non-equilibrium molecular dynamics simulations. Specifically, gold and two different materials, silicon and silica, in both their crystalline and amorphous structures, have been considered. The findings reveal that the interfacial thermal conductance between amorphous structures and gold is found to be 300% higher as compared to crystalline structures for both planar and rough interfaces ($\approx 152 \text{ MW/m}^2\text{K}$ for gold-amorphous silicon and $\approx 56 \text{ MW/m}^2\text{K}$ for gold-crystalline silicon). This threefold increase could not be captured by the diffuse mismatch model, neither be explained by phonon localization at the interface. We relate the increase of interfacial heat transfer to the enhancement of the interface bonding and the atomic displacements cross-correlations of low frequency phonons at the crystalline-amorphous interfaces. This study calls for the systematic experimental determination of the interfacial thermal conductance between amorphous materials and metals.

I. INTRODUCTION

The sharp decrease in the size of electronic devices has led to a situation where the mean-free paths of energy carriers like electrons and phonons are increasingly similar to or even exceed the characteristic length scales seen in homogeneous materials. As the size of these materials shrinks, the limited space for heat dissipation can cause localized heating effects, affecting the performance and reliability of nanoscale devices and structures. Thermal transport across interfaces is a critical factor governing effective heat transfer, which is especially true in devices with numerous material interfaces or reduced dimensions. Therefore, thermal transport across interfaces severely impedes heat dissipation, and has a significant impact on the functionality and failure point of a device [1–3]. The interfacial thermal conductance (ITC) is an important thermal quantity that determines the ability to dissipate or confine energy more efficiently at interfaces between two structures. In 1941, Kapitza measured the ITC for the first time quantitatively between solid Copper and liquid Helium [4]. As a result, in literature, ITC and "Kapitza conductance" are frequently used interchangeably. ITC can be calculated using a variety of experimental, theoretical, and computational methods. In the past few years, ITC between various metal/dielectric and dielectric/dielectric solids has been characterized thanks to the development of ultrafast measurement techniques [5, 6]. Although it is less common, ultrafast laser spectroscopy can also be used to determine the ITC between a metal and an amorphous material [7]. However, analytical predictions of the interfacial thermal transport are extremely challenging due to the anharmonicities of the interatomic forces at the inter-

face. One the main reasons for the discrepancy between the predictions of the diffuse mismatch model (DMM) [8] and acoustic mismatch model (AMM) [9] and experimental measurements at room temperature, are the exclusion of these anharmonic interactions [10]. However, molecular dynamics (MD) simulations are now recognized as one of the most effective methods for predicting ITC [11–13] especially for amorphous interfaces, as it makes no assumptions other than the classical nature of the energy carriers, which is a reasonable assumption close to and above the Debye temperature of the softer solid.

Many studies have been conducted on the investigation of ITC between a variety of crystalline-crystalline interfaces [14]. In contrast, ITC across amorphous-amorphous interfaces has not received as much attention. The low thermal conductivity of amorphous structures results in a negligible temperature drop across amorphous-amorphous interfaces, making it difficult to estimate ITC both experimentally and computationally [15]. Giri et al. and Gordiz et al. have reported high ITC of the order of $\text{GW/m}^2\text{K}$ at amorphous Si/Ge interfaces using MD simulations [15, 16]. In the case of their crystalline counterparts, MD simulations show a significant reduction in ITC [17, 18]. The main mechanisms for heat transport in these crystalline and amorphous states exhibit substantial differences. Diffusons that are non-propagating and delocalized phonon modes in the Si and Ge layers are the main heat carriers in amorphous superlattices [19]. While in contrast, for crystalline-crystalline interfaces, thermal conductance is primarily controlled by spatially extended phonon modes. As a result, the vibrational characteristics at amorphous-amorphous interfaces differ noticeably from those at crystalline-crystalline interfaces, providing insight into the significant contrast seen between the two types of interfaces. Notwithstanding the remarkable distinctions in ITC highlighted (between these interfaces), it is noteworthy to mention that there have only been a very small number of studies that have computed and

^{*} julien.el-hajj@univ-lyon1.fr

[†] samy.merabia@univ-lyon1.fr

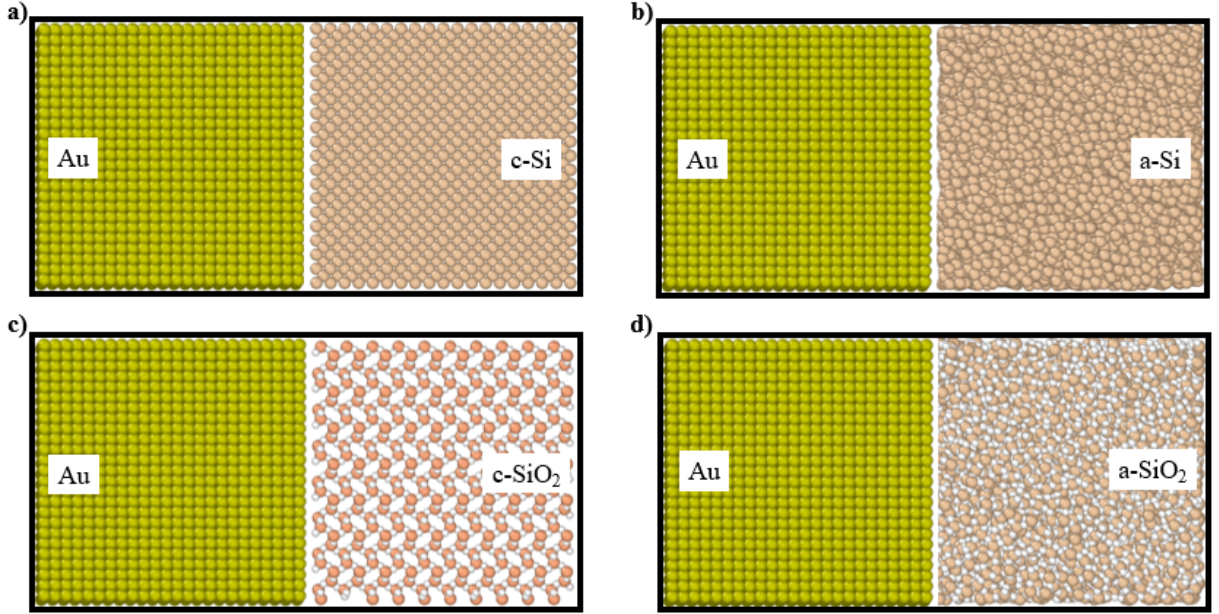


FIG. 1. Illustration of the different systems: a) gold-crystalline silicon interface, b) gold-amorphous silicon interface, c) gold-crystalline silica interface, d) gold-amorphous silica interface.

analyzed ITC for crystalline-amorphous interfaces [20]. In this article, the ITC between gold and silicon and gold and silica, respectively, is examined for both their crystalline and amorphous structural forms. We report a threefold increase in ITC when comparing the crystalline-crystalline to the crystalline-amorphous interfaces. The ITC between the gold-silicon and gold-silica systems has not been thoroughly examined although these systems have high significance and widespread use, for instance for heat transfer around core-shell nanoparticles [21]. Let us mention, however, one recent study [22] where the authors investigated ITC at the interfaces of gold and silica, and reported a double increase in ITC when comparing gold/amorphous silica to gold crystalline silica interfaces. The authors attributed this increase to a higher overlap of the vibrational density of states between amorphous silica and gold as compared to crystalline silica and gold. Here, we report a threefold increase of the ITC for gold/amorphous silicon and show that it can not be explained by the overlap between vibrational density of states. Rather, we demonstrate that the ITC enhancement is driven by the change of bonding strength at the gold-silicon interface which yields strong correlations of the atomic displacements at the interface and larger thermal flux spectrum, especially at low phonon frequencies.

II. METHODOLOGY

A. Modelling set up

Molecular dynamics (MD) simulations are performed using the Large-scale Atomic/Molecular Massively Parallel Simulator (LAMMPS) [23]. The atomic positions are integrated using the velocity Verlet algorithm with a 0.5 fs time step. The images of the simulated systems are generated using ovito software [24]. To model the interactions between silicon atoms in both crystalline and amorphous silicon structures, the Stillinger-Weber potential is employed [25]. This potential accurately reproduces both structural and vibrational properties in both structural forms. For both crystalline and amorphous silica structures, the Tersoff potential function with Munetoh et al.'s parameters [26] is used to describe the interaction between silicon and oxygen atoms. A 12 - 6 Lennard-Jones potential is employed to model the gold-gold, gold-silicon and gold-oxygen interactions with the specified parameters from Heinz et al. [27] for gold, and Rape et al. [28] for silicon and oxygen. The Lennard-Jones coefficients used at the interface are: $\epsilon_{Au-Si} = 62.5$ meV and $\sigma_{Au-Si} = 3.39$ Å for gold-silicon interactions and $\epsilon_{Au-O} = 42.9$ meV and $\sigma_{Au-O} = 3.056$ Å for gold-oxygen interactions.

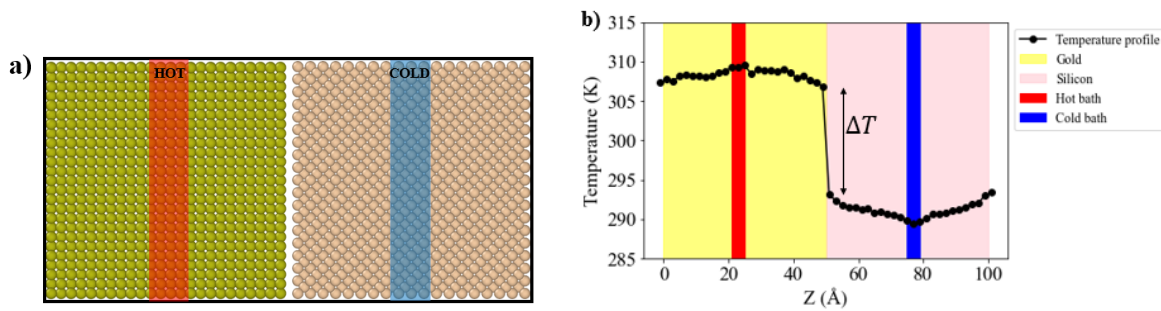


FIG. 2. a) The gold-crystalline silicon interface with its respective thermal baths used in the NEMD simulations to calculate ITC (hot bath in red and cold bath in blue). b) Temperature profile averaged from the NEMD simulation used to estimate the temperature jump at the interface.

B. Sample generation and amorphization

The interfaces under consideration are composed of gold and crystalline/amorphous silicon or silica. For crystalline silicon samples, we use periodic boundary conditions to generate systems with a diamond lattice of $a_0 = 5.43$ Å, and for crystalline silica, we use the α -Cristobalite structure with space group symmetry $P4_12_12$ and cell dimensions of $a=4.99$ Å and $c=6.93$ Å. Amorphous structures are generated using the melt-quench technique [20]. Starting with the respective crystalline structure, at 300 K, the structure is first equilibrated in the canonical ensemble. Then, within 1 ns, it is heated to 5000 K in the liquid, and held at that temperature for another 1 ns until any memory of its initial configuration is lost. The temperature is then decreased back to 300 K with a 5 K/ps rate. The resulting amorphous structures are then stabilized for 1 ns at 300 K in the canonical ensemble and the Radial Distribution Function (RDF) is computed, showing good agreement with previous simulation results in the literature [29] and with experimental measurements [30] for silicon (see supplementary information). To further validate the modelling of the amorphous structures, the bulk thermal conductivity of each system is calculated and compared with prior results. The bulk thermal conductivity of amorphous silicon is found equal to 1.44 ± 0.10 W/m.K which is in good agreement with values reported in the literature [29]; while the thermal conductivity of amorphous silica is found equal to 0.98 ± 0.09 W/m.K which is also in good agreement with values from other studies [31, 32].

C. Interfacial thermal conductance

The calculation of ITC at the gold-crystalline/amorphous interfaces is performed using non-equilibrium molecular dynamics (NEMD) by applying periodic boundary conditions along the x, y and

z directions. The Nose-Hoover equations of motion are used to integrate the atomic trajectories during all NEMD simulations [33, 34]. Figure 1 shows an example of the studied gold-crystalline silicon interfaces (a), gold-amorphous silicon interfaces (b), gold-crystalline silica interfaces (c) and gold-amorphous silica interfaces (d). Each system has a total length of 100 Å along the z direction perpendicular to the interface. In order to calculate ITC, hot and cold baths are placed in the middle of the left and right sections as shown in Figure 2a). Once the system has reached a steady state (for more details, see supplementary information), the heat flux (q) and the temperature profiles are averaged over 1 ns for ITC calculations, and the heat flux is calculated as :

$$q = \frac{dE}{dt} / 2A$$

with $\frac{dE}{dt}$, the slope of the energy supplied/extracted from the system as a function of time, and A is the surface area. ITC, expressed in $\text{W m}^{-2} \text{K}^{-1}$, computed using the ratio between the heat flux and the temperature jump at the interface (ΔT):

$$ITC = \frac{q}{\Delta T} \quad (1)$$

An example of a temperature profile from which the temperature jump at the interface is extracted is shown in Figure 2b).

III. RESULTS AND DISCUSSION

Five different simulations are run for each interface and the results for ITC are shown in table I. These findings indicate that: (1) ITC is significantly higher at gold-amorphous interfaces: we report a threefold increase in the case of silicon and twofold increase for silica. (2) The calculated ITC at the gold/crystalline silicon interface is

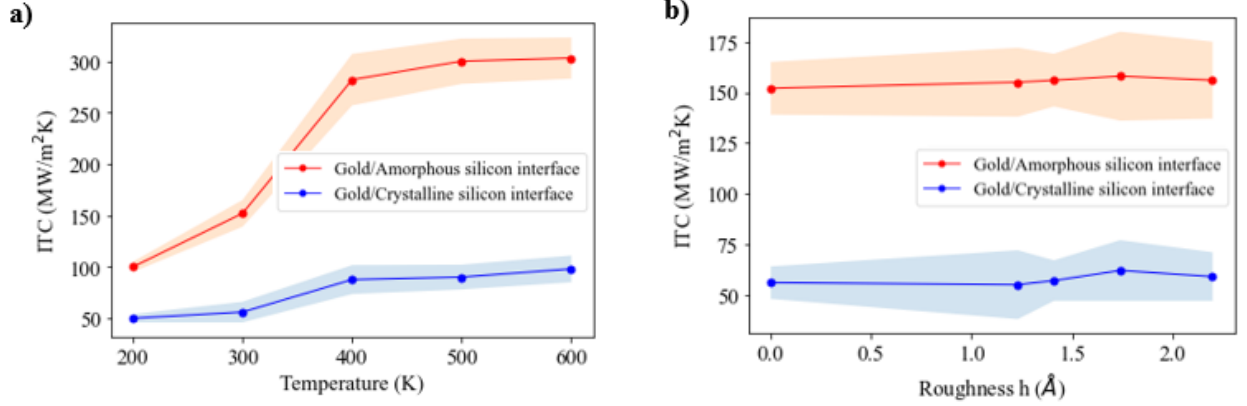


FIG. 3. a) The interfacial thermal conductance of gold/crystalline silicon and gold/amorphous silicon systems as a function of temperature. b) The interfacial thermal conductance of gold/crystalline silicon and gold/amorphous silicon systems as a function of interfacial roughness. Here the roughness is quantified by the RMS of the height distribution h at the (x,y) surface along the z direction at 300 K.

in good agreement with previous reported experimental value of ≈ 50 MW/m²K [35].

	ITC (MW/m ² K)
Gold-Amorphous Silicon	152 ± 13
Gold-Crystalline Silicon	56 ± 8

Gold-Amorphous Silica	170 ± 14
Gold-Crystalline Silica	102 ± 12

TABLE I. Values of the interfacial thermal conductance for gold/crystalline-amorphous systems. The thermal conductance is much higher at the gold-amorphous systems interfaces as compared to gold-crystalline interfaces.

We have checked that size effects are small. According to the calculated results, doubling the system length increases ITC by only 5 – 6% for all simulated interfaces (see supplementary information). Therefore, the results are almost size independent.

Moving forward, we will concentrate on the gold/crystalline silicon and gold/amorphous silicon interfaces to search for a microscopic interpretation of the threefold increase. For gold/silica interfaces, we observe qualitatively similar results.

A. Effect of temperature

The ITC values reported priorly have been calculated at 300 K. As a result, variations in the system temperature may have an impact on the results obtained and, in turn, the threefold increase observed. In order to better understand how the system average temperature affects ITC, both interfaces are simulated at different temperatures ranging between 200 and 600 K. The results are

shown in Figure 3a). The threefold increase in ITC observed at 300 K is found to be constant throughout the temperature range under consideration. ITC consistently escalates as temperatures increase. The increased anharmonic interactions at higher temperatures increases phonon transmission at the interface, resulting in higher ITC [10].

B. Effect of interfacial roughness

Real interfaces may display roughness, consequently, it is critical to address the effect of surface roughness on interfacial heat transfer [36] as it can significantly impact the threefold increase observed when comparing ITC for gold/amorphous silicon to gold/crystalline silicon. We considered a roughness along the (x,y) surface perpendicular to the z direction using a self-affine scaling transformation and the root mean square (RMS) of a height distribution h [37].

The ITC is represented in Figure 3b) as a function of the RMS of the height distribution h at 300 K. The results shows unequivocally that surface roughness had little effect on the enhancement of ITC. It is clear that the differences observed were not significant when contrasting simulations with planar interfaces with those that consider a rough interface. In other words, the outcomes were fairly comparable and did not show significant differences. This result shows that the behavior of the investigated interfaces was not significantly affected by the presence of surface roughness.

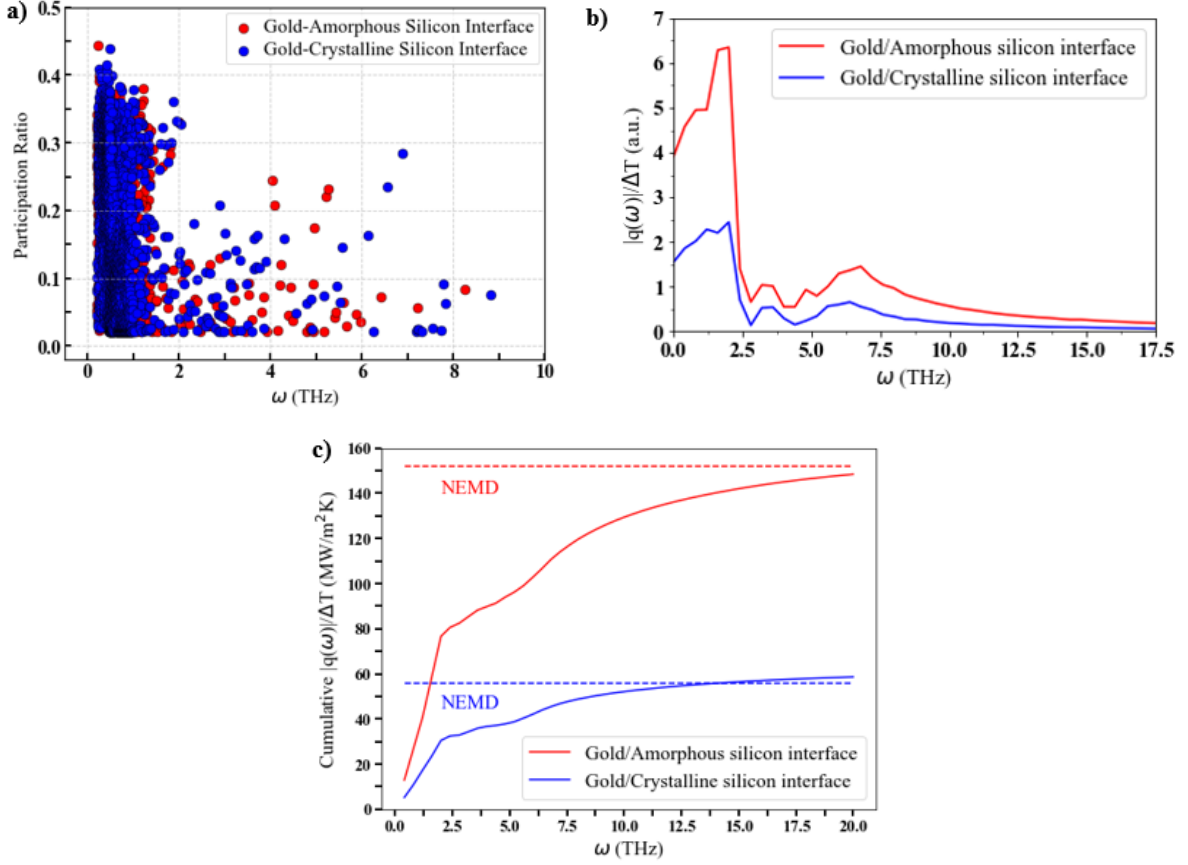


FIG. 4. a) Modal participation ratio as a function of frequency at the interface of gold/crystalline silicon (blue), and at the interface of gold/amorphous silicon (red). b) Frequency-dependent thermal flux at the gold/crystalline silicon and gold/amorphous silicon interfaces at 300 K. c) ITC calculated from the cumulative frequency-dependent thermal flux at 300 K compared with the NEMD values.

C. Failure of the diffuse mismatch model

We discuss now whether the ITC enhancement can be captured by the diffuse mismatch model (DMM) [38] and compare the obtained results with those calculated from NEMD simulations. In Landauer framework of interfacial transport, the phonon-phonon interfacial thermal conductance is given by [39]:

$$G_p = \frac{1}{2} \sum_p \int_0^{\omega_{Au,p}^c} v_{Au,p} \hbar \omega D_{Au,p}(\omega) \frac{\partial f_{eq}(\omega, T)}{\partial T} \times \int_0^{\pi/2} \alpha_p(\omega, \cos \theta) \cos \theta d(\cos \theta) d\omega$$

where the sum runs over the polarizations p , $\omega_{Au,p}^c$ denotes the cutoff frequency for gold, $v_{Au,p}$ is the group velocity of gold in the mode p , $D_{Au,p}(\omega)$ represents the bulk density of states of gold, f_{eq} signifies the equilibrium Bose-Einstein distribution, α refers to phonon transmission coefficient, and in the frame of diffuse interfacial scattering, the transmission coefficient no longer depends

on the scattering angle and is assumed to be polarization independent, it can be calculated as [38]:

$$\alpha = \frac{\sum_p \frac{1}{v_{Si}^2}}{\sum_p \frac{1}{v_{Si}^2} + \sum_p \frac{1}{v_{Au}^2}}$$

The longitudinal and transverse values of gold mode group velocity are 3390 m/s and 1290 m/s, respectively. The mode group velocities of bulk silicon structures, both crystalline and amorphous, are extracted from the calculation of the dynamical structure factor of each bulk using the Dynasor library [40] (see supplementary information). Using the DMM formalism described above, the ITC of gold/crystalline silicon is found to be equal to 82.7 (MW/m²K) which is in fair agreement with previous calculated value using DMM (≈ 86 MW/m²K) [39], while the ITC of gold/amorphous silicon is 110 (MW/m²K). This small difference between the ITC values is expected since we found there are no significant differences in the computed vibrational density of states at the two interfaces (see supplementary information).

The findings show a significant difference in the outcomes obtained using the NEMD and DMM approaches. DMM not only predicts a higher ITC value for the gold/crystalline silicon interface, but it also does not predict a threefold difference in comparison to the gold/amorphous silicon interface. This significant disparity can be attributed to the simplicity of DMM assumptions, particularly the use of a transmission coefficient which ignores the interface structure, as opposed to NEMD's comprehensive treatment of the interface and inelastic phonon transport.

D. Interface phonon localization

Another possible explanation of the difference in ITC is the localization of phonons in the vicinity of amorphous structures. This phenomenon has been indeed invoked to explain the relative high ITCs at amorphous-amorphous interfaces [19]. To understand the large increase in ITC between gold-crystalline and gold-amorphous interfaces, we investigate the localization properties of phonons in the vicinity of crystalline and amorphous structures. Unlike in crystalline structures, thermal transport in amorphous materials is related to propagons (propagating modes) and diffusons (nonpropagating modes), both of which are delocalized modes [41]. Delocalized phonon modes are the main heat carriers in amorphous interfaces and the primary cause of high ITC across amorphous interfaces [19]. Whereas in the crystalline counterparts, spatially extended modes contribute primarily to thermal transport.

In order to investigate the properties of phonons in the vicinity of the interfaces presented in this study, the modal participation ratio of phonons is calculated as follows [42]:

$$P(\mathbf{k}, \nu) = \frac{1}{N_b \sum_1^{N_b} \left(\sum_{\alpha}^3 e_{i,\alpha}^*(\mathbf{k}, \nu) e_{i,\alpha}(\mathbf{k}, \nu) \right)^2} \quad (2)$$

where N_b is the total number of atoms at the interface, where the interface is defined as the region within a cut-off radius distance (10 Å) from each side, and $e_i(k, \nu)$ is the component of the eigenmode (k, ν) relative to atom i 's coordinate. Each mode takes into account the contributions of all the atoms near the interface. The smaller the $P(k, \nu)$, the fewer atoms involved in the motion of a specific mode. More precisely, $P(k, \nu)$ equals unity when all atoms participate in a specific mode. When only one atom contributes to a mode, $P(k, \nu)$ equals $1/N_b < 1$. Figure 4a) shows no significant differences between the modal participation ratio calculated at both interfaces. In fact, only low frequency modes are populated for both interfaces, implying that only low frequencies are contributing to ITC. Furthermore, $P(k, \nu) \downarrow 0.5$ at both interfaces, indicating that phonons are strongly localized at the interface. Briefly, low frequency, strongly localized phonon modes contribute to the gold-amorphous

interfaces high ITC, despite not being associated with nonpropagating and delocalized phonon modes, as for amorphous-amorphous interfaces [16].

E. Frequency dependent thermal spectrum

We now quantify the contribution of low-frequency modes to the interfacial heat transfer at both interfaces. To this end, we computed the frequency-dependent thermal flux encodes the combined information on potential energy and vibrational density of states as follows [43]:

$$q(\omega) = \frac{2}{A} \text{Re} \left[\sum_{i \in Au} \sum_{j \in Si} \int_0^{t_{\max}} \langle F_{ij}(\tau) \cdot v_i(0) \rangle e^{i\omega\tau} d\tau \right] \quad (3)$$

where A is the surface area, F_{ij} is the force applied on the gold atom i as a result of its interaction with silicon atom j , v_i is the velocity of atom i , $\langle F_{ij}(\tau) \cdot v_i(0) \rangle$ is the correlation function between these two quantities, τ is the correlation time, and t_{\max} is the maximum time. The frequency-dependent heat flux measures the heat flux transferred between two adjacent materials as a function of frequency, giving indications on the dominant frequency range for interfacial heat transfer.

Alternately, ITC can be defined as the cumulative integral of the frequency dependent thermal spectrum as:

$$ITC = \frac{1}{\Delta T} \int_0^{w_{\max}} q(\omega') d\omega' \quad (4)$$

with ΔT , the temperature jump at the interface, and w_{\max} , the maximum calculated frequency. Figure 4b) compares the frequency dependent thermal spectrum at the interface of each system at 300 K. This result confirms the previous finding that heat transfer in both interfaces is due to low-frequency phonons ($\omega < 6$ THz), as these frequencies contribute to more than 80% of the total ITC for both systems. Furthermore, the contribution of low-frequency phonons at gold/amorphous silicon interfaces is significantly higher than at gold-crystalline silicon interfaces. This increased contribution as well as the contribution of the higher frequency modes, results in a higher ITC, which can explain the observed threefold increase but does not provide any physical interpretation of the enhancement.

Furthermore, Figure 4c) shows good agreement between the cumulative integrals of the frequency dependent thermal spectrum calculated using Equation (4) and the NEMD values.

F. Spring stiffness and atomic displacement cross-correlations thermal spectrum

To obtain further insight in the physical significance and microscopic quantities underlying the observed threefold increase, we relate now ITC to the interaction

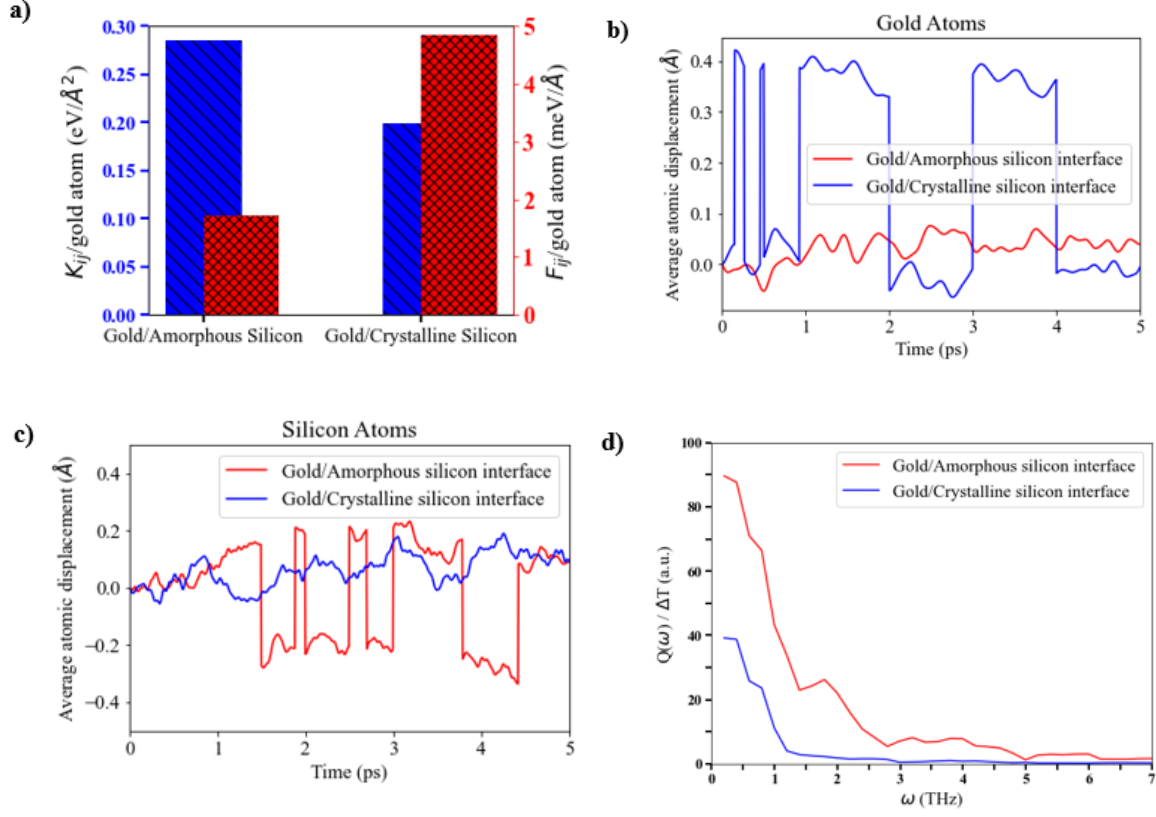


FIG. 5. a) Histograms of the average spring stiffness (blue) and forces (red) acting on a gold atom at the interface between gold/crystalline silicon, and at the interface of gold/amorphous silicon. Average atomic displacement of the selected gold-silicon pairs at the gold/crystalline silicon and gold/amorphous silicon interfaces: b) gold atoms, c) silicon atoms. d) Frequency-dependent spring stiffness and atomic displacements cross-correlations thermal flux at the gold/crystalline silicon and gold/amorphous silicon interfaces.

spring stiffness and the atomic displacements at the interface.

First, the net forces acting on a gold atom can be calculated as: $F_{ij} = -\frac{\partial U(r_{ij})}{\partial r}$, where $U(r_{ij})$ is the inter-atomic potential used to model the interaction between a gold atom i and a silicon atom j at the interface. Figure 5a) shows the calculated average net force acting on a gold atom at both interfaces. These forces are always positive, indicating that the gold and silicon atoms have a net repulsive interaction. However, there is a significant difference in the magnitude of these forces. At the gold/crystalline silicon interface, the force is approximately 60% greater than at the gold/amorphous silicon interface. This disparity suggests that, while the forces between different constituent atoms is repulsive, the gold/crystalline silicon interface corresponds to a significantly stronger repulsion. In addition, assuming harmonic interactions between the gold atoms and the silicon atoms near the interface, the interatomic forces can be approximated by a set of harmonic springs. The effective spring constant, which is proportional to the coupling between neighboring atoms, can be calculated as follows: $k_{ij} = \frac{\partial^2 U(r_{ij})}{\partial r^2}$. As a result, the stronger the coupling, the

higher the spring stiffness. Figure 5a) shows that the calculated average spring stiffness acting on a gold atom at the interface is about 30% greater at the gold-amorphous interfaces as compared to gold-crystalline interfaces.

We quantify now the effect of enhanced bonding on the atomic displacements at the interface. To this end, we calculate the cross-correlation coefficient between atomic vibrational displacements which is defined as [44]:

$$r = \frac{\sum_{i=1}^n (u_i - \bar{u})(v_i - \bar{v})}{\sqrt{\sum_{i=1}^n (u_i - \bar{u})^2} \cdot \sqrt{\sum_{i=1}^n (v_i - \bar{v})^2}} \quad (5)$$

We select the gold-silicon atom pairs n that are at their equilibrium distance once the system is fully equilibrated satisfying: $r_{Au-Si} = 2^{\frac{1}{6}} \sigma_{Au-Si}$ with a variation of 0.5 \AA , where u and v represent the atomic displacement of the gold and silicon atoms respectively. Figures 5b) and c) shows the average atomic displacement of the selected gold-silicon pairs. The cross-correlation coefficient between atomic vibrational displacements in the ideal cases is close to one, when u and v belong to the identical atom

type, indicating thermal resonance, whereas it is close to zero when the displacements between are uncorrelated. As a result, high interfacial thermal conductance can be associated with a larger thermal flux, which is directly influenced by thermal resonance [45]. The calculated cross-correlation coefficient, r , between atomic vibrational displacements is 0.128 for gold/crystalline silicon interfaces and 0.23 for gold/amorphous interfaces, which amounts approximately to a factor 2. The average atomic displacement of a gold atom at both interfaces shown in Figure 5b) is consistent with the previous result of the calculated average spring stiffness acting on a gold atom in Figure 5a). A higher spring stiffness implies stronger bonding between atoms, resulting in smaller atomic displacements from their equilibrium positions. While for silicon atoms, the average atomic displacement at both interfaces are indeed in the same distance range as shown in Figure 5c).

To relate the enhanced bonding and the cross-correlation between atomic vibrational displacements to the ITC increase, we start from the expression of the heat flux spectrum in an out of equilibrium situation:

$$\langle \tilde{Q}_{B \rightarrow A}(\omega) \rangle = \sum_{\substack{i \in Au \\ j \in Si}} \langle \tilde{F}_{ij}(\omega) \cdot \tilde{V}_i^*(\omega) \rangle \quad (6)$$

Where \sim denotes Fourier transform, $\langle \dots \rangle$ an ensemble average, \tilde{F}_{ij} is the Fourier transform of the interatomic force between atoms i and j , and $*$ denotes complex conjugate.

In the harmonic approximation, one can write:

$$\tilde{F}_{ij} = -\overleftrightarrow{K}_{ij} \cdot (\tilde{u}_i(\omega) - \tilde{u}_j(\omega)) \quad (7)$$

where $\overleftrightarrow{K}_{ij} = \frac{\partial^2 V}{\partial \vec{r}_i \partial \vec{r}_j} \bigg|_{\vec{r}_i, \vec{r}_j}$ is the Hessian of the interaction which is estimated at the equilibrium positions of the atoms, and $\vec{r}_i(\omega) = \vec{r}_i^0 + \tilde{u}_i(\omega)$, with \vec{r}_i^0 denotes the equilibrium positions and $\tilde{u}_i(\omega)$ the relative displacement.

In the harmonic limit, one has then:

$$\langle \tilde{Q}_{B \rightarrow A}(\omega) \rangle = \sum_{\substack{i \in Au \\ j \in Si}} \overleftrightarrow{K}_{ij} \cdot \langle (\tilde{u}_i(\omega) - \tilde{u}_j(\omega)) \cdot (-i\omega \tilde{u}_i^*(\omega)) \rangle \quad (8)$$

Since $\langle \tilde{Q}_{B \rightarrow A}(\omega) \rangle = -\langle \tilde{Q}_{A \rightarrow B}(\omega) \rangle$, one can obtain a symmetrized version of the thermal flux:

$$\langle \tilde{Q}(\omega) \rangle = \frac{1}{2} \left(\langle \tilde{Q}_{B \rightarrow A}(\omega) \rangle - \langle \tilde{Q}_{A \rightarrow B}(\omega) \rangle \right) \quad (9)$$

With:

$$\tilde{Q}_{A \rightarrow B}(\omega) = - \sum_{\substack{i \in Au \\ j \in Si}} \overleftrightarrow{K}_{ij} \cdot (\tilde{u}_i(\omega) - \tilde{u}_j(\omega)) \cdot (-i\omega \tilde{u}_j^*(\omega)) \quad (10)$$

Leading to:

$$\langle \tilde{Q}(\omega) \rangle = \frac{1}{2} \sum_{\substack{i \in Au \\ j \in Si}} \overleftrightarrow{K}_{ij} \cdot \langle (\tilde{u}_i(\omega) - \tilde{u}_j(\omega)) \cdot (-i\omega (\tilde{u}_i^*(\omega) + \tilde{u}_j^*(\omega))) \rangle \quad (11)$$

After developing Equation 11 the thermal flux can be expressed as:

$$Q(\omega) = \frac{-i\omega}{2} \left[\sum_{i \in Au} \sum_{j \in Si} \overleftrightarrow{K}_{ij} \cdot \langle \tilde{\Delta}_{ij}(\omega) \cdot \tilde{\Delta}_{ij}^*(\omega) \rangle \right] \quad (12)$$

with:

$$\tilde{\Delta}_{ij}(\omega) = \tilde{u}_i(\omega) - \tilde{u}_j(\omega)$$

In conclusion, we have related the thermal flux to both enhanced bonding and cross-correlation between atomic vibrational displacements. The increased interface bonding yield strong atomic displacement correlations, which together contribute to enhance the thermal spectrum. In order to estimate Equation 12, we have selected the atom pairs that are at their equilibrium distance once the system is fully equilibrated, which implies that: $r_{ij} = 2^{\frac{1}{6}} \sigma_{Au-Si}$ with a variation of 0.5 Å. Figure 5b) compares the spectrum of spring stiffness and frequency dependent atomic displacement cross-correlations at the interfaces of each system. The observed threefold increase in the gold/amorphous silicon interface is due to enhanced bonding and atomic displacement of low frequency phonon modes at the interfaces. Indeed, this analysis confirms the strong effect of moderate interface bonding on local correlations between atomic displacements at the interface and ITC.

IV. CONCLUSION

We investigated the interfacial thermal conductance at interfaces involving crystalline or amorphous silicon and silica with gold, using non-equilibrium molecular dynamics simulations. We report a substantial threefold (twofold) increase in interfacial thermal conductance specifically for gold-amorphous silicon (silica) interfaces. This noticeable enhancement was observed across both planar and atomistically rough interfaces. We showed that DMM can not capture the increase of interfacial thermal conductance as it ignores any structural feature of the interface. Phonon localization at the interfaces, which is commonly invoked to explain high ITC values at amorphous/amorphous interfaces, can not explain neither the difference between crystalline/amorphous and crystalline/crystalline systems. Rather, we showed that a moderate increase of the interface bonding leads to strong correlations between the atomic displacements at the interface resulting in higher thermal flux. We established a direct connection between the observed increase in interfacial thermal conductance and the combined effects of enhanced bonding and atomic displace-

ment cross-correlations primarily associated with low-frequency phonon modes at these interfaces. This new relation provides valuable insights into the fundamental mechanisms contributing to the augmented thermal transport across gold-amorphous solids interfaces. This study calls for the systematic experimental investigation of interfacial thermal conductance at metal-amorphous solids using e.g. thermorefectance techniques. Characterizing heat transport at these interfaces may help optimize thermal transfer around heterogeneous nanoparticles with thermoplasmonic applications.

CONFLICTS OF INTEREST

There are no conflicts of interest to declare.

ACKNOWLEDGEMENT

We thank interesting discussions with A. Rajabpour, F. Banfi, N. Horny and K. Termentzidis. This work is supported by the ANR, France project "CASTEX" ANR-21-CE30-0027-01.

DATA AVAILABILITY

The data that support the findings of this study are available from the corresponding author upon reasonable request.

-
- [1] Y. Shen, J. Gaskins, X. Xie, B. Foley, R. Cheaito, P. Hopkins, and J. Campbell, Thermal analysis of high-power flip-chip-bonded photodiodes, *Journal of Light-wave Technology* **35**, 4242 (2017).
 - [2] H.-S. P. Wong, S. Raoux, S. Kim, J. Liang, J. P. Reifenberg, B. Rajendran, M. Asheghi, and K. E. Goodson, Phase change memory, *Proceedings of the IEEE* **98**, 2201 (2010).
 - [3] D. G. Cahill, P. V. Braun, G. Chen, D. R. Clarke, S. Fan, K. E. Goodson, P. Keblinski, W. P. King, G. D. Mahan, A. Majumdar, H. J. Maris, S. R. Phillpot, E. Pop, and L. Shi, Nanoscale thermal transport. II. 2003–2012, *Applied Physics Reviews* **1**, 011305 (2014), <https://pubs.aip.org/aip/apr/article-pdf/doi/10.1063/1.4832615/14573439/011305.1.online.pdf>.
 - [4] P. L. Kapitza, Heat transfer and superfluidity of helium ii, *Phys. Rev.* **60**, 354 (1941).
 - [5] D. Cahill, W. Ford, K. Goodson, G. Mahan, A. Majumdar, H. Maris, R. Merlin, and S. Phillpot, Nanoscale thermal transport, *Journal of Applied Physics* **93**, 793 (2003).
 - [6] H.-K. Lyeo and D. G. Cahill, Thermal conductance of interfaces between highly dissimilar materials, *Phys. Rev. B* **73**, 144301 (2006).
 - [7] V. Juvé, M. Scardamaglia, P. Maioli, A. Crut, S. Merabia, L. Joly, N. Fatti, and F. Vallée, Cooling dynamics and thermal interface resistance of glass-embedded metal nanoparticles, *Physical Review B* **80** (2009).
 - [8] G. L. POLLACK, Kapitza resistance, *Rev. Mod. Phys.* **41**, 48 (1969).
 - [9] W. A. Little, The transport of heat between dissimilar solids at low temperatures, *Canadian Journal of Physics* **37**, 334 (1959), <https://doi.org/10.1139/p59-037>.
 - [10] K. Sääskilähti, J. Oksanen, J. Tulkki, and S. Volz, Role of anharmonic phonon scattering in the spectrally decomposed thermal conductance at planar interfaces, *Phys. Rev. B* **90**, 134312 (2014).
 - [11] D. G. Cahill, W. K. Ford, K. E. Goodson, G. D. Mahan, A. Majumdar, H. J. Maris, R. Merlin, and S. R. Phillpot, Nanoscale thermal transport, *Journal of Applied Physics* **93**, 793 (2002), <https://pubs.aip.org/aip/jap/article-pdf/93/2/793/10625286/793.1.online.pdf>.
 - [12] E. S. Landry and A. J. H. McGaughey, Thermal boundary resistance predictions from molecular dynamics simulations and theoretical calculations, *Phys. Rev. B* **80**, 165304 (2009).
 - [13] S. Merabia and K. Termentzidis, Thermal conductance at the interface between crystals using equilibrium and nonequilibrium molecular dynamics, *Phys. Rev. B* **86**, 094303 (2012).
 - [14] J. Chen, X. Xu, J. Zhou, and B. Li, Interfacial thermal resistance: Past, present, and future, *Rev. Mod. Phys.* **94**, 025002 (2022).
 - [15] A. Giri, P. E. Hopkins, J. G. Wessel, and J. C. Duda, Kapitza resistance and the thermal conductivity of amorphous superlattices, *Journal of Applied Physics* **118**, 165303 (2015), <https://pubs.aip.org/aip/jap/article-pdf/doi/10.1063/1.4934511/13699145/165303.1.online.pdf>.
 - [16] K. Gordiz and A. Henry, Phonon transport at interfaces between different phases of silicon and germanium, *Journal of Applied Physics* **121**, 025102 (2017), <https://pubs.aip.org/aip/jap/article-pdf/doi/10.1063/1.4973573/13223764/025102.1.online.pdf>.
 - [17] T. Murakami, T. Hori, T. Shiga, and J. Shiomi, Probing and tuning inelastic phonon conductance across finite-thickness interface, *Applied Physics Express* **7**, 121801 (2014).
 - [18] K. Gordiz and A. Henry, Phonon transport at interfaces: Determining the correct modes of vibration, *Journal of Applied Physics* **119**, 015101 (2016), <https://pubs.aip.org/aip/jap/article-pdf/doi/10.1063/1.4939207/14104444/015101.1.online.pdf>.
 - [19] A. Giri and P. E. Hopkins, A review of experimental and computational advances in thermal boundary conductance and nanoscale thermal transport across solid interfaces, *Advanced Functional Materials* **30**, 1903857 (2020), <https://onlinelibrary.wiley.com/doi/pdf/10.1002/adfm.201903857>.
 - [20] A. France-Lanord, S. Merabia, T. Albaret, D. Lacroix, and K. Termentzidis, Thermal properties of amorphous/crystalline silicon superlattices, *Journal of Physics: Condensed Matter* **26**, 355801 (2014).
 - [21] A. Alkurdi, J. Lombard, F. Detchevery, and S. Merabia, Enhanced heat transfer with metal-dielectric core-shell

- nanoparticles, *Phys. Rev. Appl.* **13**, 034036 (2020).
- [22] S. M. Hatamlee, F. Jabbari, and A. Rajabpour, Interfacial thermal conductance between gold and SiO_2 : A molecular dynamics study, *Nanoscale and Microscale Thermophysical Engineering* **26** (2022).
- [23] A. P. Thompson, H. M. Aktulga, R. Berger, D. S. Bolintineanu, W. M. Brown, P. S. Crozier, P. J. in 't Veld, A. Kohlmeyer, S. G. Moore, T. D. Nguyen, R. Shan, M. J. Stevens, J. Tranchida, C. Trott, and S. J. Plimpton, LAMMPS - a flexible simulation tool for particle-based materials modeling at the atomic, meso, and continuum scales, *Comp. Phys. Comm.* **271**, 108171 (2022).
- [24] A. Stukowski, Visualization and analysis of atomistic simulation data with OVITO-the Open Visualization Tool, *MODELLING AND SIMULATION IN MATERIALS SCIENCE AND ENGINEERING* **18**, 10.1088/0965-0393/18/1/015012 (2010).
- [25] F. H. Stillinger and T. A. Weber, Erratum: Computer simulation of local order in condensed phases of silicon [*phys. rev. b* 31, 5262 (1985)], *Phys. Rev. B* **33**, 1451 (1986).
- [26] S. Munetoh, T. Motooka, K. Moriguchi, and A. Shintani, Interatomic potential for Si-O systems using Tersoff parameterization, *Computational Materials Science* **39**, 334 (2007).
- [27] H. Heinz, R. A. Vaia, B. L. Farmer, and R. R. Naik, Accurate simulation of surfaces and interfaces of face-centered cubic metals using 12-6 and 9-6 Lennard-Jones potentials, *The Journal of Physical Chemistry C* **112**, 17281 (2008), <https://doi.org/10.1021/jp801931d>.
- [28] A. K. Rappe, C. J. Casewit, K. S. Colwell, W. A. I. Goddard, and W. M. Skiff, UFF, a full periodic table force field for molecular mechanics and molecular dynamics simulations, *Journal of the American Chemical Society* **114**, 10024 (1992), <https://doi.org/10.1021/ja00051a040>.
- [29] J. M. Larkin and A. J. H. McGaughey, Thermal conductivity accumulation in amorphous silica and amorphous silicon, *Phys. Rev. B* **89**, 144303 (2014).
- [30] K. Laaziri, S. Kycia, S. Roorda, M. Chicoine, J. L. Robertson, J. Wang, and S. C. Moss, High-energy x-ray diffraction study of pure amorphous silicon, *Phys. Rev. B* **60**, 13520 (1999).
- [31] W. Zhu, G. Zheng, S. Cao, and H. He, Thermal conductivity of amorphous SiO_2 thin film: A molecular dynamics study, *Scientific Reports* **8** (2018).
- [32] Z. Huang, Z. Tang, J. Yu, and S. Bai, Thermal conductivity of amorphous and crystalline thin films by molecular dynamics simulation, *Physica B: Condensed Matter* **404**, 1790 (2009).
- [33] S. Nosé, A unified formulation of the constant temperature molecular dynamics methods, *J. Chem. Phys.* **81**, 511 (1984).
- [34] W. G. Hoover, Canonical dynamics: Equilibrium phase-space distributions, *Phys. Rev. A* **31**, 1695 (1985).
- [35] R. Cheaito, J. T. Gaskins, M. E. Caplan, B. F. Donovan, B. M. Foley, A. Giri, J. C. Duda, C. J. Szejewski, C. Constantin, H. J. Brown-Shaklee, J. F. Ihlefeld, and P. E. Hopkins, Thermal boundary conductance accumulation and interfacial phonon transmission: Measurements and theory, *Phys. Rev. B* **91**, 035432 (2015).
- [36] S. Merabia and K. Termentzidis, Thermal boundary conductance across rough interfaces probed by molecular dynamics, *Phys. Rev. B* **89**, 054309 (2014).
- [37] H. Iteney, J. A. Gonzalez Joa, C. Le Bourlot, T. W. Cornelius, O. Thomas, and J. Amodeo, Pyrough: A tool to build 3d samples with rough surfaces for atomistic and finite-element simulations, *Computer Physics Communications* **295**, 108958 (2024).
- [38] E. T. Swartz and R. O. Pohl, Thermal boundary resistance, *Rev. Mod. Phys.* **61**, 605 (1989).
- [39] J. Lombard, F. Detcheverry, and S. Merabia, Influence of the electron-phonon interfacial conductance on the thermal transport at metal/dielectric interfaces, *Journal of physics. Condensed matter : an Institute of Physics journal* **27**, 015007 (2014).
- [40] E. Fransson, M. Slabanja, P. Erhart, and G. Wahnström, A tool for extracting dynamical structure factors and current correlation functions from molecular dynamics simulations, *Advanced Theory and Simulations* **4**, 10.1002/adts.202000240 (2021).
- [41] P. B. Allen, J. L. Feldman, J. Fabian, and F. Wooten, Diffusons, locons and propagons: Character of atomic vibrations in amorphous Si , *Philosophical Magazine B* **79**, 1715 (1999).
- [42] D. Donadio and G. Galli, Atomistic simulations of heat transport in silicon nanowires, *Phys. Rev. Lett.* **102**, 195901 (2009).
- [43] K. Sääskilahti, J. Oksanen, J. Tulkki, and S. Volz, Spectral mapping of heat transfer mechanisms at liquid-solid interfaces, *Phys. Rev. E* **93**, 052141 (2016).
- [44] J. L. Rodgers and W. A. Nicewander, Thirteen ways to look at the correlation coefficient, *The American Statistician* **42**, 59 (1988), <https://doi.org/10.1080/00031305.1988.10475524>.
- [45] X. Li, W. Chen, and G. Nagayama, Interfacial thermal resonance in an SiC-SiC nanogap with various atomic surface terminations, *Nanoscale* **15**, 8603 (2023).